PHYSICAL REVIEW B VOLUME 30, NUMBER 9 1 NOVEMBER 1984

Theoretical studies of elementary excitations in liquid ^{4}He

E. Manousakis and V. R. Pandharipande
Department of Physics and Materials Research Laboratory, University of Illinois at Urbana—Champaign, 1110 West Green Street, Urbana, Illinois 61801

(Received 7 May 1984)

Elementary excitations of liquid ^{4}He have been studied in the past with either perturbation theory in the basis of Feynman phonon states, or with variational theory using Feynman-Cohen (FC) wave functions. We develop perturbation theory in the basis of FC phonon states. Such a theory appears to have much better convergence. The second-order corrections to the FC spectrum are calculated, and these improve the agreement with experiment very significantly. We also calculate the strength $Z(k)$ of the collective mode. The second-order corrections to the $Z(k)$ of FC phonons also improve the agreement with experiment. Calculations are carried out at pressures of 0, 10, and 24 atm using the variational, Green's-function Monte Carlo and experimental pair distribution functions. Corrections to the Kirkwood superposition approximation for the three- and four-particle distribution functions are calculated with the variational ground-state wave functions containing pair and triplet correlations.

I. INTRODUCTION

During the last three decades many theoretical attempts have been made to understand the elementary excitations of liquid ^{4}He. The first ideas were given by Landau, working on the superfluid properties of liquid ^{4}He, and by Bogoliubov, who studied the dilute Bose gas. The first ansatz for the wave function of the collective excitation of momentum $\vec{k}$ was the Bijl-Feynman form:

$$|\Psi_{\vec{k}}\rangle=\rho_F(\vec{k})\,|\Psi_0\rangle\;, \tag{1.1}$$

$$\rho_F(\vec{k})=\sum_{i=1}^{N} e^{i\vec{k}\cdot\vec{r}_i}\;. \tag{1.2}$$

Here $|\Psi_0\rangle$ is the exact ground state. This wave function gives an upper bound,

$$e(k)<e_F(k)=\frac{\hbar^2}{2m}\frac{k^2}{S(k)}\;, \tag{1.3}$$

to the excitation spectrum $e(k)$. The $S(k)$ denotes the static structure function.

In their pioneering work Feynman and Cohen[1] (FC) improved the calculation of $e(k)$ significantly by incorporating the backflow in the wave function:

$$|\Psi_{\vec{k}}\rangle=\rho_B(\vec{k})\,|\Psi_0\rangle\;, \tag{1.4}$$

$$\rho_B(\vec{k})=\sum_{i=1}^{N} e^{i\vec{k}\cdot\vec{r}_i}\left[1+i\sum_{j\neq i}^{N}\eta(r_{ij})\vec{k}\cdot\vec{r}_{ij}\right]\;. \tag{1.5}$$

The function $\eta(r)$ represents the backflow velocity potential, and it is to be determined variationally; FC took $\eta(r)=A/r^3$. The excitation energy $e_B(k)$ is given by

$$e_B(k)=\frac{\hbar^2}{2m}\sum_{i=1}^{N}\frac{\langle\Psi_0|[\vec{\nabla}_i\rho_B^\dagger(\vec{k})]\cdot[\vec{\nabla}_i\rho_B(\vec{k})]|\Psi_0\rangle}{\langle\Psi_0|\rho_B^\dagger(\vec{k})\rho_B(\vec{k})|\Psi_0\rangle}\;, \tag{1.6}$$

and we need to know the two-, three-, and four-particle distribution functions to calculate it exactly. Only the two-body $g(r)$ is experimentally known.

Padmore and Chester[2] (PC) used the Monte Carlo method to calculate the two expectation values in (1.6), using the Jastrow approximation

$$|\Psi_0\rangle=\prod_{1\leq i<j\leq N} f_J(r_{ij}) \tag{1.7}$$

for the ground state. Their results are $\sim 20\%$ above the experimental values. Later Schmidt and Pandharipande[3] (SP) included three-body correlations in the $|\Psi_0\rangle$ and calculated $e_B(k)$ using hypernetted-chain summation methods. They found a small improvement in the roton region, but the calculated maxon energies were too high.

Pursuing another approach, Feenberg and collaborators[4] studied the $e(k)$ using perturbation theory in correlated basis functions (CBF). The nonorthogonal CBF are defined as

$$|n(\vec{k}_1),n(\vec{k}_2),\ldots,n(\vec{k}_m)\rangle=\prod_{i=1}^{m}[\rho_F(\vec{k}_i)]^{n(\vec{k}_i)}|\Psi_0\rangle\;; \tag{1.8}$$

they include one- and many-phonon states. The unperturbed (zeroth-order) spectrum is the Bijl-Feynman $e_F(k)$. There are no first-order contributions in CBF theory. Jackson and Feenberg[5] studied the Brillouin-Wigner second-order contribution from two-phonon intermediate states, and later Lee and Lee[6] included the second-order effects of three-phonon states. In these calculations the Jastrow approximation was used for the ground state. CBF calculations using $|\Psi_0\rangle$ containing two- and three-body correlations were performed by Chang and Campbell.[7] When Bijl-Feynman phonons are used to construct the CBF, the zeroth-order $e_F(k)$ is $\sim 2e(k)$, and the perturbative corrections are large. It is difficult to push the CBF perturbation theory beyond the leading- (second-) order corrections.

In this paper we consider the next obvious step of using CBF generated with the FC $\rho_B(\vec{k})$ operators. The zeroth-order spectrum is much closer to the $e(k)$ in this basis, and we find that the leading perturbative corrections are not too hard to calculate when a short-ranged $\eta(r)$ is used. The perturbative corrections are smaller in this basis, and the expansion is expected to have a much better convergence.

In Sec. II A we report variational calculations of $e_B(k)$ with the Jastrow approximation for the ground state. The PC calculation is repeated using hypernetted-chain summation methods, and a possible sign error is pointed out. The spectrum is studied with both long- and short-ranged $\eta(r)$, and it is not too sensitive to the long-range tail of $\eta(r)$. The calculations are much simpler with the short range $\eta(r)$. The effect of three-body correlations in the ground state are studied in Sec. II B. It is shown that the Feynman-Cohen roton energies may be $\sim 10\%$ higher than those obtained by PC or SP.

The second-order CBF correction is calculated in Sec. III, and in Sec. IV we discuss the calculation of the strength Z_k of the collective mode:

$$Z_k = | \langle \Psi_0 | \rho_F^\dagger(\vec{k}) | \Psi_{\vec{k}} \rangle |^2 , \tag{1.9}$$

in the dynamic form factor $S(k,\omega)$. The phonon wave functions used in the calculation of Z_k include the second-order CBF corrections.

The results are presented in Sec. V. The experimental $g(r)$ is used, and the microscopic theory is used to calculate only the corrections to the Kirkwood superposition approximation for the three- and four-body distribution functions. We find that the small perturbative corrections significantly reduce the gap between the variational FC theory and experiment. The spectra calculated with the experimental $g(r)$ are in good agreement with the data, but those obtained with either the variational or the Green's-function Monte Carlo $g(r)$ overestimate the $e(k)$ in some region of k by $\sim 15\%$.

II. VARIATIONAL CALCULATIONS

In the first part of this section we discuss calculations with the Jastrow ground state. McMillan and optimum Jastrow correlations[8] are used, with the long-ranged $\eta_L(r) = A_L/r^3$ of FC, and the short-ranged $\eta_S(r)$:

$$\eta_S(r) = A_S \exp\{-[(r-r_0)/w_0]^2\} , \tag{2.1}$$

used in the variational theory[9] of liquid ^{3}He, to study the spectrum. The parameters A_L, A_S, r_0, w_0 of η_L and η_S are determined variationally. In Sec. II B we use the $\eta_S(r)$ and the ground state with optimum Jastrow and triplet correlations to calculate the $e_B(k)$. The main results and conclusions of the variational calculations are summarized in Sec. II C.

A. Calculations with Jastrow ground state

We begin by evaluating the denominator of $e_B(k)$ [Eq. (1.6)]. It is convenient to use the diagrammatic notation of Fig. 1 to depict various terms of the operator $\rho_B^\dagger(\vec{k})\rho_B(\vec{k})$. The wiggly lines represent backflow correlations $i\vec{k}\cdot\vec{r}\eta(r)$, and the exchange lines represent $e^{i\vec{k}\cdot\vec{r}}$. The term $e^{i\vec{k}\cdot\vec{r}_i}$ in $\rho_B(\vec{k})$ is represented by starting the exchange line from point i, while the end of the line in the point j represents $e^{-i\vec{k}\cdot\vec{r}_j}$ in $\rho_B^\dagger(\vec{k})$. In "direct" diagrams [Fig. 1(1.1) for example] $i=j$. An angle mark at the beginning of an exchange line [Fig. 1(1.4)] indicates that the marked backflow correlation is from $\rho_B(k)$. An angle mark at the end of the exchange line [Fig. 1(1.5)] is used to denote backflow correlations from $\rho_B^\dagger(k)$.

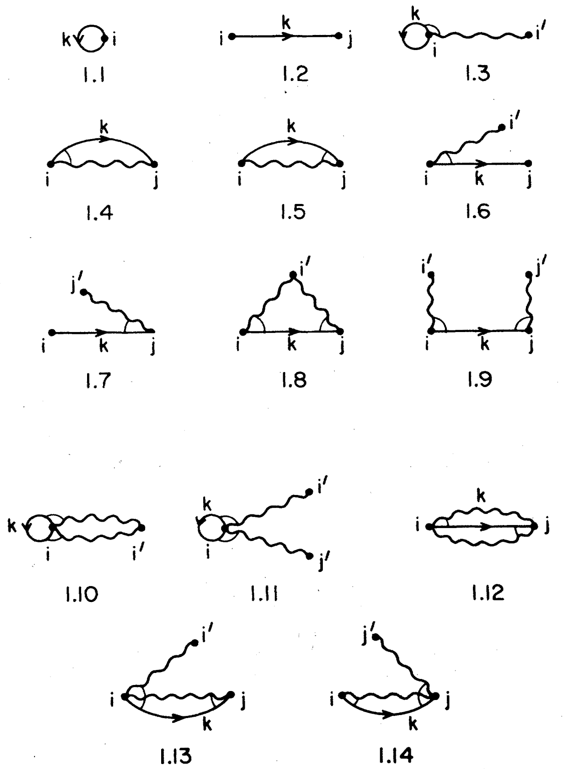

FIG. 1. Diagrams depicting all the terms in the operator $\rho_B^\dagger(\vec{k})\rho_B(\vec{k})$. The wiggly and directed lines denote, respectively, backflow correlations and exchanges.

The expectation value $\langle \Psi_0 | \rho_B^\dagger(\vec{k})\rho_B(\vec{k}) | \Psi_0 \rangle$ is obtained by multiplying the diagrams of Fig. 1 with appropriate distribution functions, powers of density, and integrating them. The two-body distribution function is denoted by g_{ij} or $g(r_{ij})$, and its calculation is discussed in Refs. 8 and 10. The three-body distribution function can be written as

$$g_{3,ijk} = g_{ij} g_{jk} g_{ki} (1 + A_{ijk}) , \tag{2.2}$$

where A_{ijk} denotes the contribution of Abe diagrams. Terms such as $g_{ij}g_{jk}$ can be extracted from $g_{3,ijk}$ by replacing g_{ki} with $1+(g_{ki}-1)$. Such terms give factorizable diagrams as discussed below. Since $g \sim 1$ except at small r, the factorizable diagrams have importance. The four-particle distribution function is approximated by

$$g_{4,ijkl} = g_{ij} g_{jk} g_{kl} g_{li} g_{ik} g_{jl} (1 + A_{ijk} + A_{jkl} + A_{kli} + A_{lij}) . \tag{2.3}$$

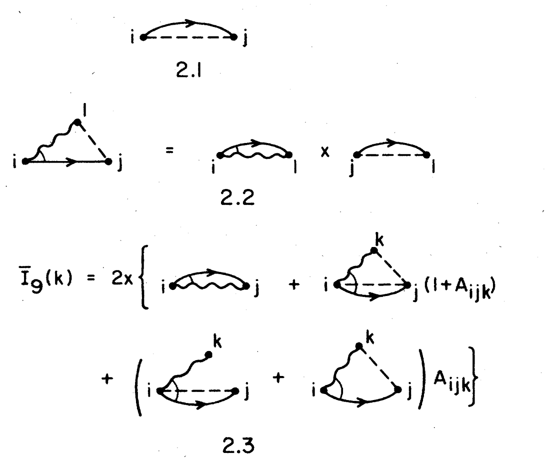

FIG. 2. Some of the diagrams contributing to the denominator $e_B(k)$.

We neglect four-body analogs of Abe diagrams. It is unlikely that these are important.

The contribution of Fig. 1(1.1) is taken as unit; i.e., all the diagrams are divided by the number of particles N. Only the $g-1$ term contributes to Fig. 1(1.2). The nonzero part of Fig. 1(1.2) is shown in Fig. 2(2.1), where a dashed line denotes $g-1$. The sum of Fig. 1(1.1) and 1(1.2) gives the familiar structure function

$$S(k)=1+\rho \int [g(r)-1]e^{i\vec{k}\cdot\vec{r}}d^3r \ . \qquad (2.4)$$

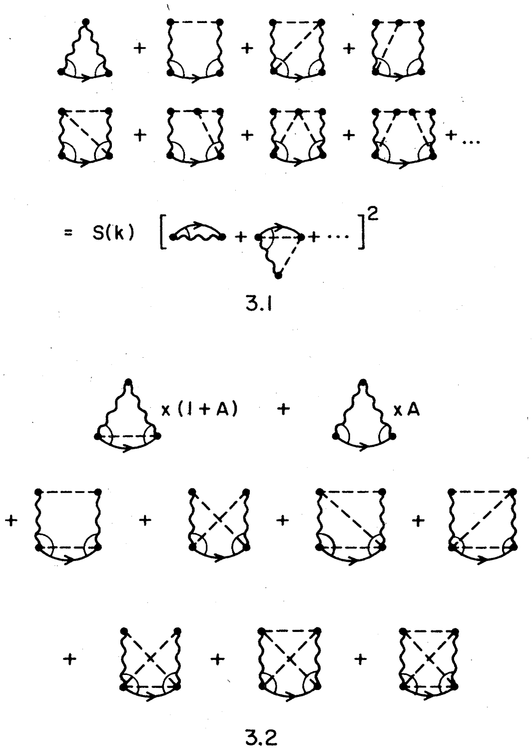

FIG. 3. Factorizable parts of Figs. 1(1.8) and 1(1.9) are shown in Fig. 3(3.1) and the unfactorizable in Fig. 3(3.2).

Figure 1(1.3) and a similar diagram having the backflow correlation from $\rho_B^\dagger(\vec{k})$, give zero contribution. Figures 1(1.4) and 1(1.5) occur as factors in the factorizable terms of three-body Figs. 1(1.6) and 1(1.7). The factorization is illustrated in Fig. 2(2.2). The sum of Figs. 1(1.4) to 1(1.7) is given by $S(k)\overline{I}_9(k)$. $\overline{I}_9$ is shown diagrammatically in Fig. 2(2.3) and is given by

$$\overline{I}_9(k)=2\rho i \int d^3r\, e^{i\vec{k}\cdot\vec{r}}\eta(r)\vec{k}\cdot\vec{r}g(r)+2\rho^2 i \int d^3r_{ij}d^3r_{ik}e^{i\vec{k}\cdot\vec{r}_{ij}}\vec{k}\cdot\vec{r}_{ik}\eta_{ik}g_{ik}[(g_{ij}-1)(g_{jk}-1)(1+A_{ijk})+(g_{ij}+g_{jk}-2)A_{ijk}] \ . \qquad (2.5)$$

The first term of $\overline{I}_9(k)$ has contributions from the $r\rightarrow\infty$ tail of the $\eta_L(r)$. These are treated as discussed by FC.

The sum of terms quadratic in $\eta(r)$ is written as

$$I_{10}(k)=S(k)[\overline{I}_9(k)]^2/4+\overline{I}_{10}(k) \ . \qquad (2.6)$$

The first term of the above expression sums the factorizable contributions of Figs. 1(1.8) and 1(1.9) as illustrated in Fig. 3(3.1). $\overline{I}_{10}(k)$ contains contributions of Figs. 1(1.10) to 1(1.14) (these have no factorizable parts), and the unfactorizable parts of Figs. 1(1.8) and 1(1.9), as illustrated diagrammatically in Fig. 3(3.2). The last two diagrams of Fig. 3(3.2) have four-body elementary structures. Their contribution is very negligible ($<1\%$). The Abe corrections to the four-body diagrams of $\overline{I}_{10}(k)$ are also expected to be small, and are neglected in this work.

Following FC, the I_{10} is divided into three parts:

$$\overline{I}_{10}(k)=[I_3+I_3^{\text{ex}}(k)+I_{11}(k)]k^2 \ . \qquad (2.7)$$

I_3k^2 is the sum of Figs. 1(1.10) and 1(1.11),

$$I_3=(4\pi\rho/3) \int dr\, r^4\eta^2(r)g(r)+(\rho^2/3) \int d^3r_{ij}\, d^3r_{ik}\, \hat{r}_{ij}\cdot\hat{r}_{ik}\eta_{ij}\eta_{ik}g_{ij}g_{ik}(g_{jk}-1+g_{jk}A_{ijk}) \ . \qquad (2.8)$$

$I_3^{\text{ex}}(k)k^2$ is the sum of Figs. 1(1.12)—1(1.14),

$$I_3^{\text{ex}}(k)=-\rho \int d^3r\, \eta^2(r)(\vec{r}\cdot\hat{k})^2g(r)e^{i\vec{k}\cdot\vec{r}}-2\rho^2 \int d^3r_{ij}d^3r_{ik}\eta_{ij}\eta_{ik}g_{ij}g_{ik}\vec{r}_{ij}\cdot\hat{k}\,\vec{r}_{ik}\cdot\hat{k}\,e^{i\vec{k}\cdot\vec{r}_{ij}}(g_{jk}-1+g_{jk}A_{ijk}) \ . \qquad (2.9)$$

The $I_{11}(k)k^2$ is the sum of all diagrams of Fig. 3(3.2),

$$I_{11}(k)=\rho^2 \int d^3r_{ij}d^3r_{ik}\eta_{ik}\eta_{jk}g_{ik}g_{jk}\vec{r}_{ik}\cdot\hat{k}\,\vec{r}_{jk}\cdot\hat{k}\,e^{i\vec{k}\cdot\vec{r}_{ij}}(g_{ij}-1+g_{ij}A_{ijk})$$
$$+\rho^3 \int d^3r_{ij}d^3r_{ik}d^3r_{il}\eta_{ik}\eta_{jl}g_{ik}g_{jl}\vec{r}_{ik}\cdot\hat{k}\,\vec{r}_{jl}\cdot\hat{k}\,e^{i\vec{k}\cdot\vec{r}_{ij}}[(g_{ij}-1)(g_{kl}-1)g_{il}g_{jk}+(g_{il}-1)(g_{jk}-1)(g_{ij}+g_{kl}-1)]\ . \tag{2.10}$$

FC approximate the entire $I_{10}(k)$ [Eq. (2.6)] by k^2I_3.

Collecting all terms together we find

$$\langle\Psi_0|\rho_B^\dagger(\vec{k})\rho_B(\vec{k})|\Psi_0\rangle/N=[1+\bar{I}_9(k)/2]^2S(k)+\bar{I}_{10}(k)\ . \tag{2.11}$$

When the short-range $\eta_S(r)$ is used, the contribution of all the four-body irreducible terms of Fig. 3(3.2) to the above expectation value is $<1\%$. When the long-range $\eta_L(r)$ is used, the first two four-body diagrams have large contributions that partly cancel those of the first three-body diagram of Fig. 3(3.2), and one of the diagrams (1.13) and (1.14) of Fig. 1. These four-body chain diagrams get most of their contribution from the long-range tails of $\eta_L(r)$. This contribution is not affected by the Abe terms. The rest of the four-body diagrams have $<1\%$ contribution even for $\eta_L(r)$. Thus it appears that the Abe corrections to the four-body distribution function can be safely neglected.

FC divide the numerator of $e_B(k)$ into eight terms:

$$\langle\Psi_0|[\vec{\nabla}_i\rho_B^\dagger(\vec{k})]\cdot[\vec{\nabla}_i\rho_B(\vec{k})]|\Psi_0\rangle=k^2(1+I_1+I_2+k^2I_3+I_4+I_5+kI_6+I_7)\ . \tag{2.12}$$

These are shown in Fig. 4 with the following diagrammatic notation. An arrow on a wiggly line denotes $\vec{\nabla}_i$ operating on the $i\eta(r)\vec{k}\cdot\vec{r}$. The ∇_i can operate on the $e^{i\vec{k}\cdot\vec{r}}$ exchange lines, but this is not explicitly shown in the diagrams. All diagrams contributing to the expectation value (2.12) must have two gradients, thus diagrams with 0, 1, or 2 gradients of the $i\eta(r)\vec{k}\cdot\vec{r}$ must have 2, 1, and 0 derivatives of exchange lines, respectively. Only the direct diagrams contribute to terms in which both gradients operate on the $e^{i\vec{k}\cdot\vec{r}}$. These diagrams are not shown in Fig. 4. They look exactly like the diagrams (1.1), (1.10), and (1.11) of Fig. 1, and their contribution is $k^2(1+k^2I_3)$.

I_1, I_2, and I_6 contain terms with one $\vec{\nabla}_i\eta(r)\vec{k}\cdot\vec{r}$. We obtain

$$I_1=2\rho \int d^3r\,g(r)\hat{k}\cdot\vec{\nabla}[\eta(r)\hat{k}\cdot\vec{r}]\ , \tag{2.13}$$

$$I_2=-2\rho \int d^3r\,g(r)e^{i\vec{k}\cdot\vec{r}}\hat{k}\cdot\vec{\nabla}[\eta(r)\hat{k}\cdot\vec{r}]\ , \tag{2.14}$$

$$I_6=-\rho \int d^3r\,g(r)\eta(r)\hat{k}\cdot\vec{r}\hat{k}\cdot\vec{\nabla}[\eta(r)\hat{k}\cdot\vec{r}]i(e^{i\vec{k}\cdot\vec{r}}-e^{-\vec{k}\cdot\vec{r}})$$
$$-\rho^2 \int d^3r_{ij}d^3r_{il}g_{ij}g_{il}\eta_{il}\hat{k}\cdot\vec{r}_{il}\hat{k}\cdot\vec{\nabla}_i(\eta_{ij}\hat{k}\cdot\vec{r}_{ij})i(e^{i\vec{k}\cdot\vec{r}_{ij}}-e^{-i\vec{k}\cdot\vec{r}_{ij}})(g_{jl}-1+g_{jl}A_{ijl})\ . \tag{2.15}$$

The tail of $\eta_L(r)$ contributes to I_1 and I_2 as discussed by FC.

The I_4, I_5, and I_7 contain terms in which both gradients operate on the backflow correlations. The three-body diagrams of these terms (Fig. 4) have a factorizable part. We find

$$I_4+I_5+I_7=\tfrac{1}{4}(I_1+I_2)^2+\rho \int d^3r\{[\vec{\nabla}[\eta(r)\hat{k}\cdot\vec{r}]\}^2g(r)(2-e^{i\vec{k}\cdot\vec{r}}-e^{-i\vec{k}\cdot\vec{r}})$$
$$+\rho^2 \int d^3r_{ij}d^3r_{il}\vec{\nabla}_i(\eta_{ij}\hat{k}\cdot\vec{r}_{ij})\cdot\vec{\nabla}_i(\eta_{il}\hat{k}\cdot\vec{r}_{il})g_{ij}g_{il}(1+e^{i\vec{k}\cdot\vec{r}_{jl}}-e^{i\vec{k}\cdot\vec{r}_{ij}}-e^{-i\vec{k}\cdot\vec{r}_{ij}})(g_{jl}-1+g_{jl}A_{ijl})\ . \tag{2.16}$$

The scaling approximation,[8]

$$A_{ijk}=\left[1+\frac{s}{2}\right]\rho \int d^3r_m(g_{im}-1)(g_{jm}-1)(g_{km}-1)\ , \tag{2.17}$$

is used for A_{ijk}. The scaling parameter s is taken from Refs. 8 and 10. The calculated spectra are shown in Fig. 5, where $e_F(k)$-O is the Bijl-Feynman spectrum obtained with the optimized Jastrow ground state; $e_B(k)$-LO and $e_B(k)$-SO are with the η_L and η_S using the optimized Jastrow ground state; and $e_B(k)$-LM is with the η_L and the McMillan-Jastrow ground state.

The $e_B(k)$-LM has been calculated by PC with the Monte Carlo method.[2] Their results differ from ours; for example PC values for the roton minimum are $k=1.75$ Å and $\Delta=11.2\pm0.5$ K against our $k=1.75$ Å and $\Delta=13.2$ K. However, this difference is not due to our use of the scaling approximation to calculate distribution functions. In fact we could reproduce all their integrals other than the I_6. Our calculation gives $I_6(k)$ of similar magnitude but opposite in sign to their (PC, Fig. 1). If we change the sign of our I_6, we reproduce PC results accurately (Δ becomes 11.3 K). We note that at small k the leading two-body integral of $I_6(k)$ [Eq. (2.15)] becomes

$$-\tfrac{32}{15}\pi\rho \int dr\,r^4\eta_L^2(r)g(r)\ , \tag{2.18}$$

and it is definitely negative, while the PC $I_6(k)$ is positive at small k. Secondly, it may be verified that the sign of I_6 in the FC paper (see equation for I_{6a}, Ref. 1, page 1199) is also wrong. However, FC neglect I_6 so their results are not affected.

The optimum values of the parameters of $\eta_S(r)$ are

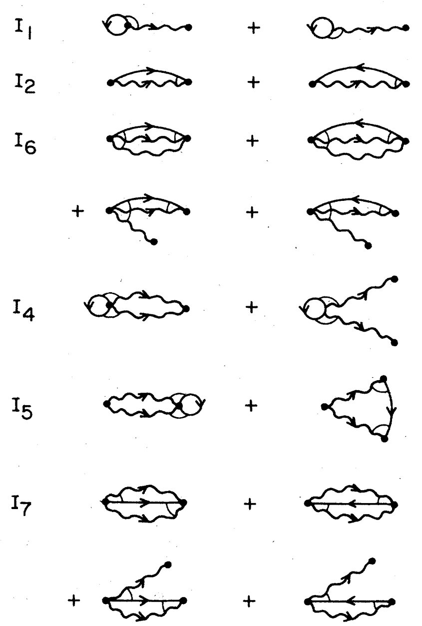

FIG. 4. Diagrams depicting all the terms in the operator $[\vec{\nabla}\rho_B^\dagger(\vec{k})\cdot\vec{\nabla}\rho_B(\vec{k})]$.

$$A_S=0.15\ ,\quad r_0=0.8\sigma\ ,\quad w_0=0.44\sigma\ . \tag{2.19}$$

The spectrum obtained with these values is very close to that obtained by minimizing $e_B(k)$-SO at each value of k by varying the A_S, r_0 and w_0. The parameter A_L of η_L has significant k dependence as noted by FC. It is obvious that, from a variational point of view, η_L is superior to η_S. However, the η_S contains much of the backflow effects; it is much simpler to work with it, and it is less sensitive to k. We can hope that the CBF states generated with the η_S are much closer to the real states than the Bijl-Feynman phonon states. Hence in the following parts of this paper we restrict to η_S.

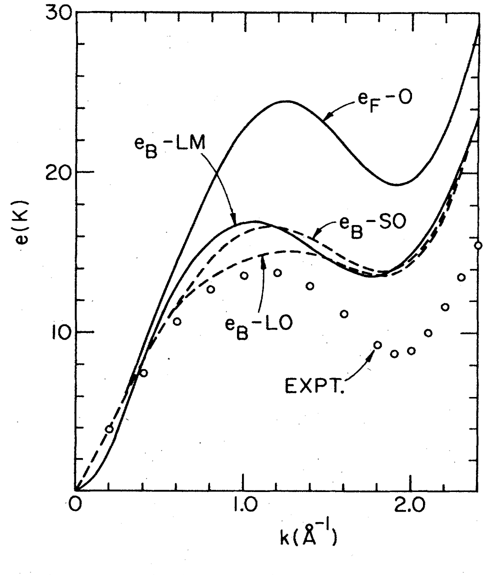

FIG. 5. Spectra calculated with Jastrow ground state. Subscripts B and F denote FC and Feynman phonons; L and S stand for long- and short-range $\eta(r)$; and M and O for the McMillan and optimized wave functions. The experimental data is from Ref. 14.

B. Three-body correlations

In this section we use the optimized Jastrow and triplet (OT) ground-state wave function:

$$\Psi_0=\prod_{i<j} f_{J,ij} \prod_{i<j<k} f_{3,ijk}\ , \tag{2.20}$$

determined in Ref. 10. The expressions for the expectation values remain the same as given in the preceding section. The only change is to add the effects of triplet correlations to the A_{ijk}:

$$A_{ijk}=f^2_{3,ijk}(A^g_{ijk}+A^t_{ijk})+f^2_{3,ijk}-1\ , \tag{2.21}$$

where A^g_{ijk} is the Abe contribution from $g-1$ bonds and A^t_{ijk} is that from $f^2_{3,ijk}-1$ bonds.

The $f_{3,ijk}$ has an effect on the two-body $g(r)$, and this is taken into account by calculating the $g(r)$ with the methods described in Ref. 10. Thus the effect of $f_{3,ijk}$ on the large two-body integrals is fully considered. However, the effect on the less important three-body irreducible diagrams is calculated approximately with

$$A_{ijk}=f^2_{3,ijk}A^g_{ijk}+A^{t1}_{ijk}+f^2_{3,ijk}-1\ , \tag{2.22}$$

where A^{t1}_{ijk} are four-body Abe diagrams with one f^2_3-1 bond. The A^{t1}_{ijk} has very small effect on the $e_B(k)$. The four-body irreducible diagrams of Fig. 3(3.2) have $<1\%$ contribution when η_S is used. Nevertheless we calculate the effect of one f^2_3-1 link on the first five "chain-type" four-body diagrams, and neglect it for the last two.

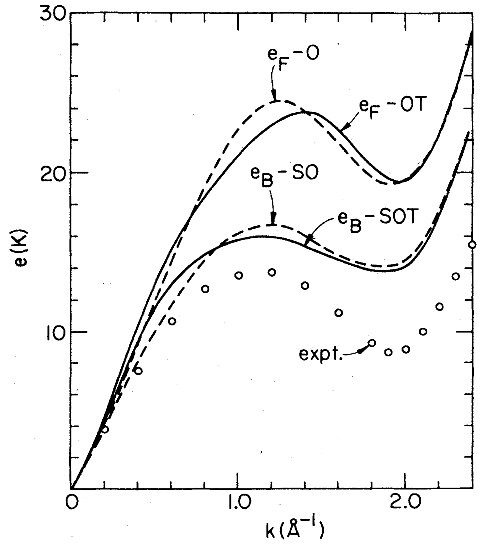

FIG. 6. Spectra calculated with ground states having optimized Jastrow (O) and optimized Jastrow plus triplet (OT) correlations.

TABLE I. FC phonon energies (in K) obtained with the short-ranged $\eta(r)$ and Jastrow plus triplet ground state, using the full calculation, two-body, and extended two-body approximations.

	$e_B(k)$		
k (Å^{-1})	Full	TB	ETB
0.2	4.4	4.4	4.4
0.4	9.8	9.6	9.8
0.6	13.20	11.75	12.65
0.8	14.91	12.05	14.53
1.0	15.86	12.40	15.30
1.2	15.98	13.00	15.49
1.4	15.47	13.58	15.28
1.6	14.63	13.81	14.70
1.8	13.87	13.74	14.12
2.0	14.17	14.55	14.57
2.2	17.00	18.15	17.52
2.4	23.04	25.57	23.64

C. Results of the variational calculations

The $e_B(k)$ and $e_F(k)$ calculated with the optimized and OT ground states are shown in Fig. 6. The OT energies are a little better than the optimized energies, but the difference is not as large as indicated by earlier calculations.[3] The main conclusion of this variational study is that the $e_B(k)$ is significantly above the experimental $e(k)$ in the maxon-roton region. Particularly for the rotons the disagreement is much worse than was believed to be.[1-3]

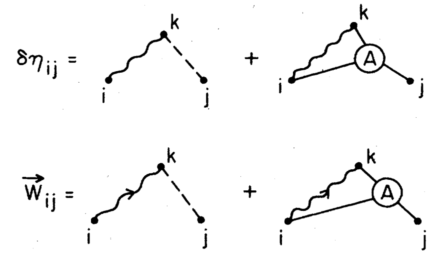

FIG. 7. Diagrammatic representation of functions $\delta\eta_{ij}$ and $\vec{W}_{ij}$ in the extended two-body approximation.

Secondly, it appears that when a short-range η_S is used, the two-body integrals give the dominant contributions to the I's. Thus the simplest approximation to calculate the expectation values in this case is to keep only the two-body integrals in the I's. The spectrum obtained in this two-body (TB) approximation is within $\sim 20\%$ of the result of the full calculation, as may be seen in Table I. Significantly improved results, with accuracy of better than 5%, are obtained by including the elements illustrated in Fig. 7 in the two-body integrals. We define

$$\delta\eta(r_{ij})=\frac{\rho}{r_{ij}^2}\int d^3r_k\,\vec{r}_{ij}\cdot\vec{r}_{ik}\eta_{ik}g_{ik}(g_{jk}-1+A_{ijk})\ , \tag{2.23}$$

$$\vec{W}(\vec{k},\vec{r}_{ij})=\rho\int d^3r_k\,\vec{\nabla}_i(\vec{k}\cdot\vec{r}_{ik}\eta_{ik})g_{ik}(g_{jk}-1+A_{ijk})\ . \tag{2.24}$$

In the extended two-body (ETB) approximation the I's are given by

$$\bar{I}_9(k)=2\rho i\int d^3r\,e^{i\vec{k}\cdot\vec{r}}\{\eta(r)g(r)+\delta\eta(r)[g(r)-1]\}\ , \tag{2.25}$$

$$I_3=\frac{\rho}{3}\int d^3r\,r^2g(r)\eta(r)[\eta(r)+\delta\eta(r)]\ , \tag{2.26}$$

$$I_3^{\text{ex}}(k)=-\rho\int d^3r[\eta(r)+\delta\eta(r)]^2(\vec{r}\cdot\hat{k})^2g(r)e^{i\vec{k}\cdot\vec{r}}\ , \tag{2.27}$$

$$I_6(k)=-\rho\int d^3r\,g(r)[\eta(r)+\delta\eta(r)](\hat{k}\cdot\vec{r})\hat{k}\cdot\vec{\nabla}[\hat{k}\cdot\vec{r}\eta(r)]i(e^{i\vec{k}\cdot\vec{r}}-e^{-i\vec{k}\cdot\vec{r}})\ , \tag{2.28}$$

$$\begin{aligned}I_4+I_5+I_7=&\tfrac{1}{4}(I_1+I_2)^2+\rho\int d^3r\,g(r)\vec{\nabla}[\hat{k}\cdot\vec{r}\eta(r)]\cdot\vec{\nabla}[\hat{k}\cdot\vec{r}\eta(r)]\\&+\rho\int d^3r\,\vec{\nabla}[\hat{k}\cdot\vec{r}\eta(r)]\cdot\{\vec{\nabla}[\hat{k}\cdot\vec{r}\eta(r)]+\vec{W}(\hat{k},\vec{r})\}(1-e^{i\vec{k}\cdot\vec{r}}-e^{i\vec{k}\cdot\vec{r}})\ ,\end{aligned} \tag{2.29}$$

$I_{11}=0$, and I_1 and I_2 [Eqs. (2.13) and (2.14)] remain unchanged. The spectrum calculated with ETB approximation is given in Table I. It is much simpler to calculate the CBF correction in this approximation.

We conclude this section with a discussion of the spectrum in the limit $k\to 0$. In this limit, as noted by FC, the backflow correlations are irrelevant. When we use $\eta_S(r)$ the $\bar{I}_9$ and $\bar{I}_{10}$ are, respectively, linear and quadratic in k, and the leading term of the denominator is $S(k)$. The leading term of the numerator is $\hbar^2k^2/2m$, and $e_B(k\to 0)$ is simply $\hbar^2k^2/2mS(k)$. With $\eta_L(r)$, the integrals I_1, I_2, and $\bar{I}_9$ become, respectively, $8\pi\rho A_L/3$, $8\pi\rho A_L/3$, and $16\pi\rho A_L$ in the $k\to 0$ limit. In this case also we obtain

$$e_B(k\to 0)=\frac{\hbar^2}{2m}\frac{k^2}{S(k)}\frac{[1+\frac{1}{2}(I_1+I_2)]^2}{(1+\frac{1}{2}\bar{I}_9)^2}=\frac{\hbar^2}{2m}\frac{k^2}{S(k)}\ . \tag{2.30}$$

It may be noted that I_1 and I_2 do not cancel in the $k\to 0$ limit as assumed by FC.

III. CBF PERTURBATION CALCULATIONS

In this section we generalize the CBF perturbation theory[4–7] to include backflow correlations and calculate the second-order corrections to $e^{(2)}(k)$ from two-phonon states $|\Psi_{lm}\rangle$:

$$
\begin{aligned}
|\Psi_{lm}\rangle &= \dot{\rho}_B(\vec{l})\dot{\rho}_B(\vec{m})|\Psi_0\rangle \\
&\equiv \sum_{j,n\,(j\neq n)} e^{i\vec{l}\cdot\vec{r}_j}\left[1+i\sum_{j'\,(\neq j)}\vec{l}\cdot\vec{r}_{jj'}\eta_{jj'}\right]e^{i\vec{m}\cdot\vec{r}_n}\left[1+i\sum_{n'\,(\neq n)}\vec{m}\cdot\vec{r}_{nn'}\eta_{nn'}\right]|\Psi_0\rangle\,, \qquad (3.1)
\end{aligned}
$$

where the overdots denote the $(j\neq n)$ restriction in two-phonon states. This state is orthogonalized to the one-phonon state having momentum $\vec{k}=\vec{l}+\vec{m}$ and normalized as follows:

$$|\vec{k}\rangle \equiv \rho_B(\vec{k})|\Psi_0\rangle/\langle\Psi_0|\rho_B^\dagger(\vec{k})\rho_B(\vec{k})|\Psi_0\rangle^{1/2}\,, \qquad (3.2)$$

$$|\vec{l},\vec{m}\rangle = \frac{|\Psi_{lm}\rangle - |\vec{k}\rangle\langle\vec{k}|\Psi_{lm}\rangle}{\langle\Psi_{lm}|\Psi_{lm}\rangle^{1/2}}\,. \qquad (3.3)$$

The second-order Brillouin-Wigner correction to the phonon energy is given by

$$e^{(2)}(k)=\frac{1}{2}\sum_{\vec{l}\,(\neq\vec{0},\vec{k})}\frac{|\langle\vec{l},\vec{m}|(H-E_0)|\vec{k}\rangle|^2}{e_B(k)+e^{(2)}(k)-e_B(l)-e_B(m)}\,. \qquad (3.4)$$

The matrix element in Eq. (3.4) is conveniently written as

$$\langle\vec{l},\vec{m}|(H-E_0)|\vec{k}\rangle = \frac{H_{lm,k}N_{k,k}-H_{k,k}N_{lm,k}}{N_{k,k}(N_{k,k}N_{lm,lm})^{1/2}}\,, \qquad (3.5)$$

where

$$H_{lm,k}=\frac{\hbar^2}{2m}\sum_p\langle\Psi_0|\vec{\nabla}_p[\dot{\rho}_B^\dagger(\vec{l})\dot{\rho}_B^\dagger(\vec{m})]\cdot\vec{\nabla}_p\rho_B(\vec{k})|\Psi_0\rangle\,, \qquad (3.6)$$

$$N_{lm,k}=\langle\Psi_0|\dot{\rho}_B^\dagger(l)\dot{\rho}_B^\dagger(\vec{m})\rho_B(\vec{k})|\Psi_0\rangle\,, \qquad (3.7)$$

$$N_{lm,lm}=N_{l,l}N_{m,m}\cdots\,. \qquad (3.8)$$

The new matrix elements to be calculated are $N_{lm,k}$ and $H_{lm,k}$. We first discuss the calculation of $N_{lm,k}$. The operator,

$$\dot{\rho}_B^\dagger(\vec{m})\dot{\rho}_B^\dagger(\vec{l})\rho_B(\vec{k})$$

contains eight terms as shown in Fig. 8. The k line ending in i denotes a factor $\exp(i\vec{k}\cdot\vec{r}_i)$, while the l and m lines starting from j and n, respectively, denote $\exp(-i\vec{l}\cdot\vec{r}_j)$ and $\exp(-i\vec{m}\cdot\vec{r}_n)$. Each of the eight terms of Fig. 8 are shown as disconnected pieces. Diagrams contributing to $N_{lm,k}$ are obtained by connecting these pieces directly or via $g-1$ or Abe correlation bonds. The points of connection will be called common points.

For example, the first term of Fig. 8 gives all the connected diagrams of Fig. 9(9.1). Since $\vec{k}=\vec{l}+\vec{m}$, we can represent the diagrams of Fig. 9(9.1) by those of Fig. 9(9.2). In the TB approximation we sum the first six diagrams of Fig. 9(9.2). The contributions of these can be written as products of two-body integrals. The contributions of the last diagrams and the Abe diagrams cannot be factored into a product of two-body integrals. These three-body irreducible diagrams are expected to have small contributions and we neglect them. This approximation is equivalent to the convolution approximation used by Feenberg[4] to calculate CBF matrix elements with Bijl-Feynman phonon states. Diagrams whose contribu-

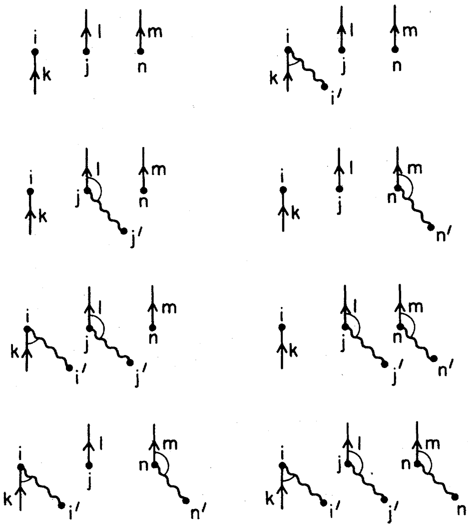

FIG. 8. Diagrams depicting all the terms of the operator $\dot{\rho}_B^\dagger(\vec{m})\dot{\rho}_B^\dagger(\vec{l})\rho_B(\vec{k})$.

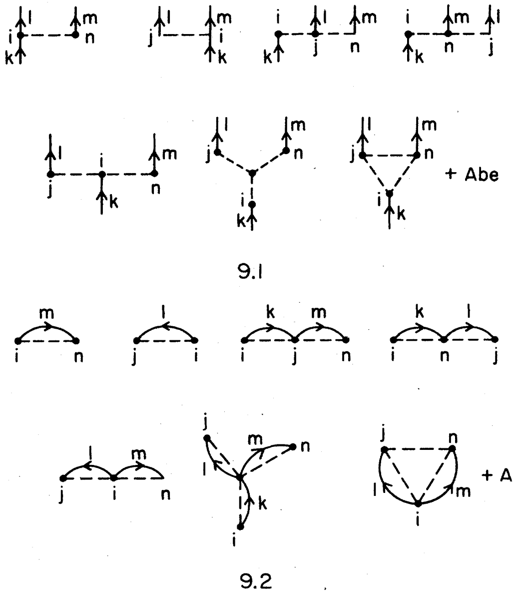

FIG. 9. All diagrams, with only $g-1$ bonds, that contribute to $N_{lm,k}$.

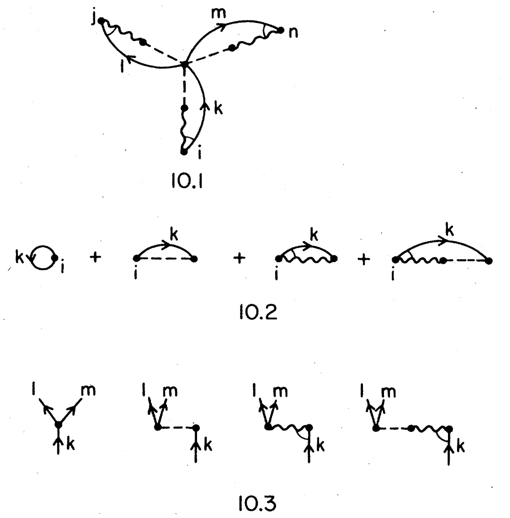

FIG. 10. $N_{lm,k}$ diagrams of class I.

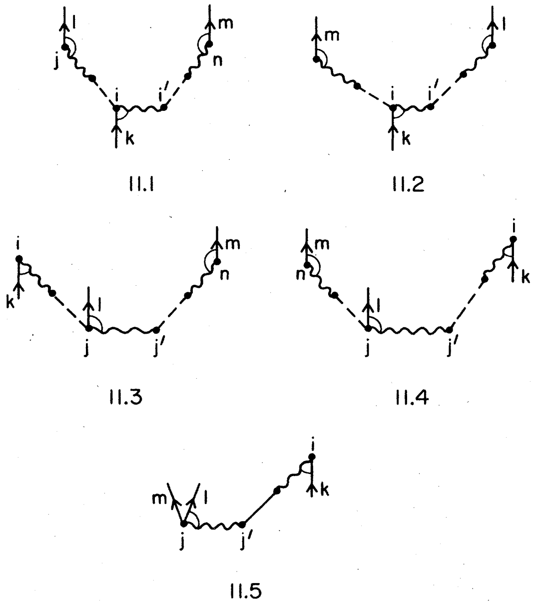

FIG. 11. $N_{lm,k}$ diagrams of class II.

tion can be expressed as a product of two-body integrals will be called TBF diagrams.

The TBF diagrams are divided into four classes. The first contains all the diagrams in which none of the points with an angle marking is a common point. The most complicated of these is shown in Fig. 10(10.1). Others of this class are obtained by shortening the branches meeting at the common point. The possible branches are shown in Fig. 10(10.2). The diagrams illustrated in Fig. 10(10.3) are not allowed due to our $j \neq n$ restriction in the two-phonon wave function [Eq. (3.1)], and so the l and m branches cannot be simultaneously eliminated. We define $S_B(k)$ as the sum of the four diagrams of Fig. 10(10.2):

$$S_B(k)=S(k)[1+\tfrac{1}{2}\bar{I}_{9,2}(k)] , \tag{3.9}$$

where $\bar{I}_{9,2}(k)$ is simply the TB part of $\bar{I}_9(k)$ [Eq. (2.5)]. The sum of the 60 diagrams belonging to this class is obtained as

$$\Sigma_1=S_B(k)[S_B(l)S_B(m)-1] . \tag{3.10}$$

In the ETB approximation we replace $\bar{I}_{9,2}$ with the $\bar{I}_9$ given by Eq. (2.25).

In the second class we have diagrams in which one of the points having an angle marking is a common point. Since this point can be either i, j, or n, we have three subclasses denoted by Σ_{2i}, Σ_{2j}, and Σ_{2n}. The most complicated diagrams of subclass Σ_{2i} are shown in Figs. 11(11.1) and 11(11.2). Others can be obtained by shortening the branches starting from points i and i'. All these diagrams have $\vec{k}\cdot\vec{r}_{ii'}\eta(r_{ii'})$, and their sum is given by

$$\Sigma_{2i}=\frac{1}{2}\left[\frac{\vec{k}\cdot\vec{m}}{m^2}\bar{I}_{9,2}(m)+\frac{\vec{k}\cdot\vec{l}}{l^2}\bar{I}_{9,2}(l)\right]S_B(m)S_B(l) . \tag{3.11}$$

Figures 11(11.3) and 11(11.4) belong to Σ_{2j}. We can shorten the branches starting from j and j' to obtain other diagrams, however, the m branch of Fig. 11(11.4) cannot be eliminated completely since Fig. 11(11.5) is not allowed. We obtain

$$\begin{aligned}\Sigma_{2j}=&-\frac{1}{2}\frac{\vec{l}\cdot\vec{m}}{m^2}\bar{I}_{9,2}(m)S_B(k)S_B(m)\\&+\frac{1}{2}\frac{\vec{k}\cdot\vec{l}}{k^2}\bar{I}_{9,2}(k)S_B(k)[S_B(m)-1] .\end{aligned} \tag{3.12}$$

The Σ_{2n} is obtained by interchanging $\vec{m}$ and $\vec{l}$ in Σ_{2j}, and expressions in the ETB approximation are obtained by replacing $\bar{I}_{9,2}$ with $\bar{I}_9$.

The third class has diagrams in which two points with angle markings are common points. Again there are three subclasses: Σ_{3ij}, Σ_{3jn}, and Σ_{3ni}. Diagrams contributing to Σ_{3jn} are illustrated in Figs. 12(12.1) and 12(12.2). They give

$$\Sigma_{3jn}=\rho S_B(k)\int d^3r\, g(r)\eta^2(r)(\vec{m}\cdot\vec{r})(\vec{l}\cdot\vec{r})(e^{i\vec{m}\cdot\vec{r}}+e^{i\vec{l}\cdot\vec{r}}) . \tag{3.13}$$

Examples of Σ_{3ij} diagrams are shown in Figs. 12(12.3) to 12(12.6). We obtain

$$\begin{aligned}\Sigma_{3ij}=&\rho S_B(m)\int d^3r\, g(r)\eta^2(r)(\vec{k}\cdot\vec{r})(\vec{l}\cdot\vec{r})(e^{i\vec{m}\cdot\vec{r}}-e^{i\vec{l}\cdot\vec{r}})\\&+\rho[S_B(m)-1]\int d^3r\, g(r)\eta^2(r)(\vec{k}\cdot\vec{r})(\vec{l}\cdot\vec{r})-\rho[S_B(m)-1]\int d^3r g(r)\eta^2(r)\vec{k}\cdot\vec{r}\,\vec{l}\cdot\vec{r}e^{i\vec{k}\cdot\vec{r}} .\end{aligned} \tag{3.14}$$

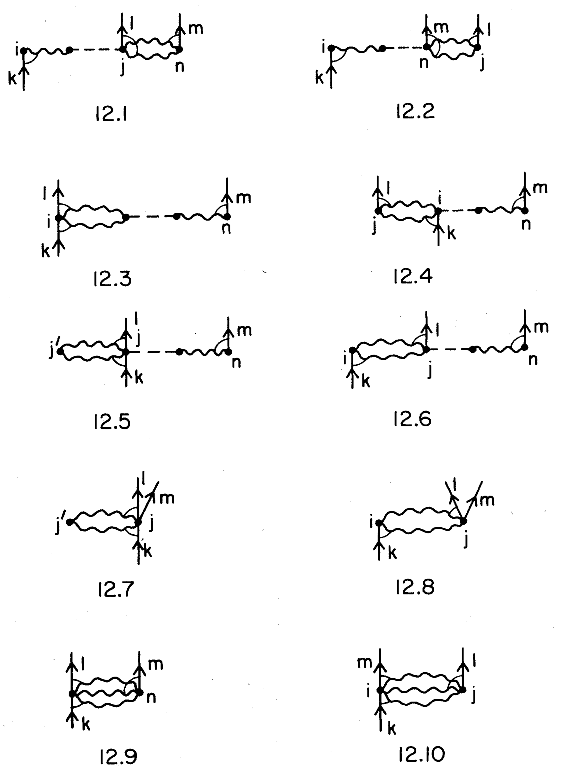

FIG. 12. $N_{lm,k}$ diagrams of classes III and IV.

The -1 in $[S_B(m)-1]$ removes the contribution of diagrams of type 12(12.7) and 12(12.8) are not allowed.

The Σ_{3in} is obtained by exchanging l and m in Σ_{3ij}. In the ETB approximation we replace the η^2 in Eq. (3.13) and in the first and third terms of Eq. (3.14) by $(\eta+\delta\eta)^2$, and that in the second term of Eq. (3.14) with $(\eta+\delta\eta)\eta$.

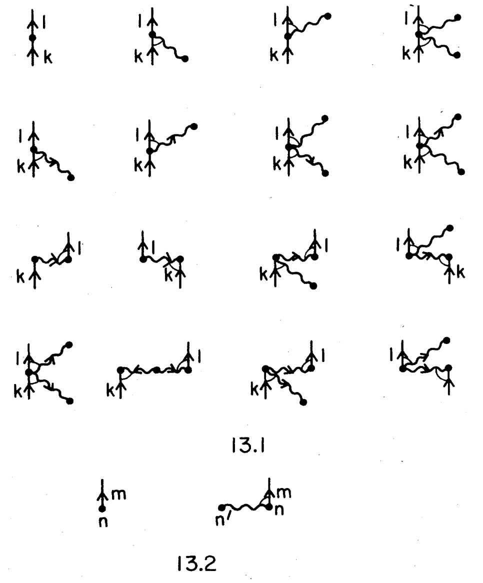

FIG. 13. Diagrams depicting all the terms in the operator $\dot\rho_B^\dagger(\vec m)[\vec\nabla\dot\rho_B^\dagger(\vec l)]\cdot[\vec\nabla\rho_B(\vec k)]$ are obtained by linking one of the two diagrams (13.2) to any of the sixteen diagrams in Fig. 13(13.1).

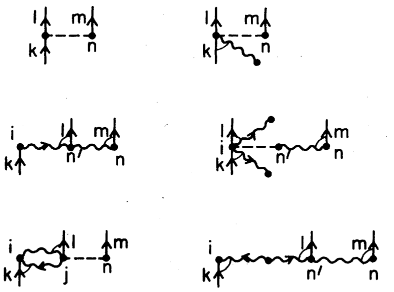

FIG. 14. $H_{lm,k}$ diagrams of class I.

The fourth class contains just the two diagrams in Figs. 12(12.9) and 12(12.10). These contain integrals of $\eta^3(r)g(r)$, and are expected to be small. We neglect them. The $N_{lm,k}$ is approximated by

$$N_{lm,k}=\Sigma_1+\Sigma_{2k}+\Sigma_{2j}+\Sigma_{2n}+\Sigma_{3ij}+\Sigma_{3jn}+\Sigma_{3ni}\ . \qquad (3.15)$$

The matrix element $H_{lm,k}$ is the ground-state expectation value of the operator:

$$\frac{\hbar^2}{2m}\nabla_p[\dot\rho_B^\dagger(\vec l)\dot\rho_B^\dagger(\vec m)]\cdot\nabla_p\rho_B(\vec k)\ .$$

This operator has two terms,

$$\frac{\hbar^2}{2m}\dot\rho_B^\dagger(\vec m)\vec\nabla_p\dot\rho_B^\dagger(\vec l)\cdot\vec\nabla_p\rho_B(\vec k)\ ,$$

and the other obtained by interchanging m and l. The contribution of the second is trivially obtained from that of the first. The first term itself consists of the 32 terms shown in Fig. 13. In the terms of Fig. 13(13.1), having two wiggly lines, the possibility of both wiggly lines ending in the same particle has to be considered explicitly. Connected diagrams, formed by linking a piece with the

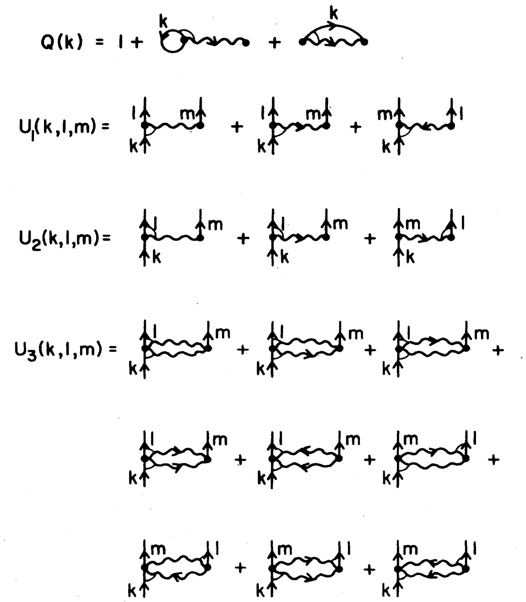

FIG. 15. Diagrammatic representation of the functions giving the contribution of $H_{lm,k}$ diagrams of class II.

m line [Fig. 13(13.2)] to the main pieces of Fig. 13(13.1), contribute to the expectation value.

The TBF diagrams are divided into three classes. The first class contains diagrams obtained by connecting n or n' with the origin of the l line. Some of these are shown in Fig. 14. Their sum is

$$T_1=\vec{k}\cdot\vec{l}\left[\frac{1}{k^2}H_{k,k}-\frac{\hbar^2}{2m}\vec{k}\cdot\vec{m}I_{3,2}\right][S_B(m)-1]\;, \qquad (3.16)$$

where $I_{3,2}$ is the two-body integral in I_3 [Eq. (2.8)], and in the ETB approximation we replace it with the I_3 of Eq. (2.25).

The second class contains diagrams formed by letting n or n' be any particle of the main piece, other than the origin of the l line; or by connecting n or n' to any particle with a $g-1$ bond. The sum of these diagrams is given by

$$T_2=[Q(l)U_1(k,l,m)+Q(k)U_2(k,l,m)+U_3(k,l,m)]S_B(m)\;. \qquad (3.17)$$

The $Q(k)$, $U_1(k,l,m)$, $U_2(k,l,m)$, and $U_3(k,l,m)$ are shown in Fig. 15. In the ETB approximation we obtain

$$Q(k)=1+\tfrac{1}{2}[I_1+I_2(k)]\;, \qquad (3.18)$$

$$\begin{aligned}U_1(k,l,m)=&\frac{\hbar^2}{2m}\vec{k}\cdot\vec{l}\rho\int d^3r\, i\vec{k}\cdot\vec{r}\{\eta(r)g(r)+\delta\eta(r)[g(r)-1]\}e^{i\vec{m}\cdot\vec{r}}\\&+\frac{\hbar^2}{2m}\rho\int d^3r\{\vec{\nabla}[\vec{k}\cdot\vec{r}\eta(r)]\cdot\vec{l}g(r)(e^{i\vec{m}\cdot\vec{r}}-e^{i\vec{l}\cdot\vec{r}})+\vec{W}(\vec{k},\vec{r})\cdot\vec{l}[g(r)-1]e^{i\vec{m}\cdot\vec{r}}\}\end{aligned} \qquad (3.19)$$

$$\begin{aligned}U_2(k,l,m)=&\frac{\hbar^2}{2m}\vec{k}\cdot\vec{l}\rho\int d^3r(-i\vec{l}\cdot\vec{r})\{\eta(r)g(r)+\delta\eta(r)[g(r)-1]\}e^{i\vec{m}\cdot\vec{r}}\\&+\frac{\hbar^2}{2m}\rho\int d^3r\{\vec{\nabla}[\vec{l}\cdot\vec{r}\eta(r)]\cdot\vec{k}g(r)(e^{i\vec{m}\cdot\vec{r}}-e^{i\vec{l}\cdot\vec{r}})+\vec{W}(\vec{l},\vec{r})\cdot\vec{k}[g(r)-1]e^{i\vec{m}\cdot\vec{r}}\}\;,\end{aligned} \qquad (3.20)$$

$$\begin{aligned}U_3(k,l,m)=&\frac{\hbar^2}{2m}\vec{k}\cdot\vec{l}\rho\int d^3r\,\vec{k}\cdot\vec{r}\vec{l}\cdot\vec{r}g(r)[\eta(r)+\delta\eta(r)]^2e^{i\vec{m}\cdot\vec{r}}\\&+\frac{\hbar^2}{2m}\rho\int d^3r\,g(r)\{-i\vec{l}\cdot\vec{r}[\eta(r)+\delta\eta(r)]\vec{D}(\vec{k},\vec{r})\cdot\vec{l}+i\vec{k}\cdot\vec{r}[\eta(r)+\delta\eta(r)]\vec{D}(\vec{l},\vec{r})\cdot\vec{k}\\&\qquad+\vec{D}(\vec{k},\vec{r})\cdot\vec{D}(\vec{l},\vec{r})+\vec{\nabla}[\vec{k}\cdot\vec{r}\eta(r)]\cdot\vec{\nabla}[\vec{l}\cdot\vec{r}\eta(r)]\}e^{i\vec{m}\cdot\vec{r}}\\&-\frac{\hbar^2}{2m}\rho\int d^3r\,g(r)\{i\vec{l}\cdot\vec{r}[\eta(r)+\delta\eta(r)]\vec{\nabla}[\vec{k}\cdot\vec{r}\eta(r)]\cdot\vec{l}+i\vec{k}\cdot\vec{r}[\eta(r)+\delta\eta(r)]\vec{\nabla}[\vec{l}\cdot\vec{r}\eta(r)]\cdot\vec{k}\\&\qquad+\vec{\nabla}[\vec{k}\cdot\vec{r}\eta(r)]\cdot\vec{D}(\vec{l},\vec{r})+\vec{D}(\vec{k},\vec{r})\cdot\vec{\nabla}[\vec{l}\cdot\vec{r}\eta(r)]\}e^{i\vec{l}\cdot\vec{r}}\;,\end{aligned} \qquad (3.21)$$

where

$$\vec{D}(\vec{k},\vec{r})=\nabla[\vec{k}\cdot\vec{r}\eta(r)]+\vec{W}(\vec{k},\vec{r})\;. \qquad (3.22)$$

The expressions for the TB approximation are trivially obtained from these, by setting $\vec{W}$ and $\delta\eta$ equal to zero.

The last class contains diagrams in which both n and n' are common points. Of these we neglect those having $\eta^3(r)g(r)$, and the sum of the rest is obtained as

$$T_3=Q(k)W_1(k,l,m)+Q(l)W_2(k,l,m)+W_3(k,l,m)\;. \qquad (3.23)$$

Diagrams contributing to W_1, W_2, and W_3 are shown in Fig. 16. We obtain

$$\begin{aligned}W_1(k,l,m)=&\frac{\hbar^2}{2m}\vec{k}\cdot\vec{l}\rho\int d^3r\,g(r)\vec{l}\cdot\vec{r}\vec{m}\cdot\vec{r}[\eta(r)+\delta\eta(r)]^2e^{i\vec{m}\cdot\vec{r}}+\frac{\hbar^2}{2m}\rho\int d^3r\,g(r)\vec{m}\cdot\vec{r}[\eta(r)+\delta\eta(r)]\vec{D}(\vec{l},\vec{r})\cdot(i\vec{k})e^{i\vec{m}\cdot\vec{r}}\\&+\frac{\hbar^2}{2m}\rho\int d^3r\,g(r)\vec{m}\cdot\vec{r}[\eta(r)+\delta\eta(r)]\vec{\nabla}[\vec{l}\cdot r\eta(r)]\cdot(i\vec{k})e^{i\vec{l}\cdot\vec{r}}\;,\end{aligned} \qquad (3.24)$$

$$\begin{aligned}W_2(k,l,m)=&-\frac{\hbar^2}{2m}\vec{k}\cdot\vec{l}\rho\int d^3r\,g(r)\vec{k}\cdot\vec{r}\vec{m}\cdot\vec{r}[\eta(r)+\delta\eta(r)]^2e^{i\vec{m}\cdot\vec{r}}\\&-\frac{\hbar^2}{2m}\rho\int d^3r\,g(r)\vec{m}\cdot\vec{r}[\eta(r)+\delta\eta(r)]\vec{D}(\vec{k}\cdot\vec{r})\cdot(-i\vec{l})e^{i\vec{m}\cdot\vec{r}}\\&-\frac{\hbar^2}{2m}\rho\int d^3r\,g(r)\vec{m}\cdot\vec{r}[\eta(r)+\delta\eta(r)]\vec{\nabla}[\vec{k}\cdot r\vec{\eta}(r)]\cdot(-i\vec{l})e^{i\vec{l}\cdot\vec{r}}\;,\end{aligned} \qquad (3.25)$$

$$W_3(k,l,m)=-\frac{\hbar^2}{2m}\rho^2\int d^3r\,g(r)\vec{\nabla}[\vec{l}\cdot\vec{r}\eta(r)]e^{i\vec{l}\cdot\vec{r}}\Big\{-i\int d^3r'g(r')\vec{m}\cdot\vec{r}'[\eta(r')+\delta\eta(r')]\vec{\nabla}[\vec{k}\cdot\vec{r}'\eta(r')]e^{i\vec{k}\cdot\vec{r}'}$$
$$+\vec{k}\int d^3r'g(r')\vec{m}\cdot\vec{r}'\vec{k}\cdot\vec{r}'\eta(r')[\eta(r')+\delta\eta(r')]\Big\}\;. \qquad (3.26)$$

The full matrix element $H_{lm,k}$ is given by adding to $T_1+T_2+T_3$ the terms obtained by interchanging $\vec{l}$ and $\vec{m}$.

IV. CALCULATION OF THE $Z(k)$

The dynamic form factor $S(k,\omega)$ at zero temperature is given by[11]

$$S(k,\omega)=Z(k)\delta(\omega-e(k))+S_m(k,\omega)\;, \qquad (4.1)$$

where the $Z(k)$ term gives the contribution of one-phonon state, and $S_m(k,\omega)$ is that of two or more phonon states. The $Z(k)$ is given by

$$Z(k)=|\langle\Psi_0|\rho_F^\dagger(\vec{k})|\Psi(\vec{k})\rangle|^2\;, \qquad (4.2)$$

where $|\Psi(\vec{k})\rangle$ is the normalized wave function of the one-phonon state.

The strength $Z_B(k)$ is calculated using the FC wave function for the phonon:

$$Z_B(k)=\frac{|\langle\Psi_0|\rho_F^\dagger(\vec{k})\rho_B(\vec{k})|\Psi_0\rangle|^2}{\langle\Psi_0|\rho_B^\dagger(\vec{k})\rho_B(\vec{k})|\Psi_0\rangle}\;. \qquad (4.3)$$

The calculation of the expectation value of $\rho_F^\dagger(k)\rho_B(k)$ differs little from that of $\langle\Psi_0|\rho_B^\dagger(\vec{k})\rho_B(\vec{k})|\Psi_0\rangle$ discussed in Sec. II. All that we have to do is to omit the terms with wiggly lines from $\rho_B^\dagger(k)$. This gives

$$\langle\Psi_0|\rho_F^\dagger(\vec{k})\rho_B(\vec{k})|\Psi_0\rangle=S(k)[1+\tfrac{1}{2}\bar{I}_9(k)]\;. \qquad (4.4)$$

The $Z_B(k)$ is the first-order result of CBF theory. In second order we use the wave function

$$|\Psi(\vec{k})\rangle=\left[|\vec{k}\rangle+\frac{1}{2}\sum_{\vec{l}\,(\neq\vec{0},\vec{k})}A_{k,lm}|\vec{l},\vec{m}\rangle\right]\Bigg/\left[1+\frac{1}{2}\sum_{\vec{l}\,(\neq\vec{0},\vec{k})}A_{k,lm}^2\right]^{1/2}, \qquad (4.5)$$

where $|\vec{k}\rangle$ and $|\vec{l},\vec{m}\rangle$ are the CBF states defined in Eqs. (3.2), (3.3), and

$$A_{k,lm}=\frac{\langle\vec{l},\vec{m}|(H-E_0)|\vec{k}\rangle}{e_B(k)+e^{(2)}(k)-e_B(l)-e_B(m)}\;. \qquad (4.6)$$

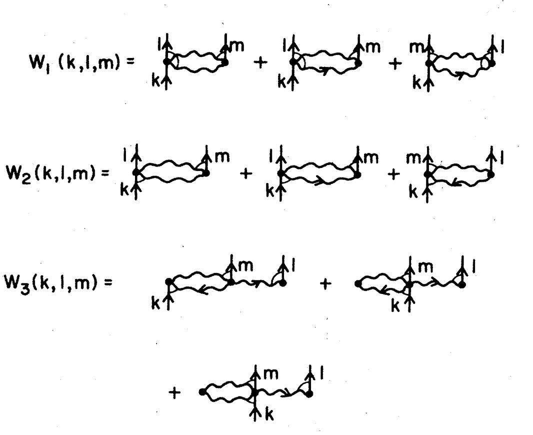

FIG. 16. Diagrammatic representation of the functions giving the contribution of $H_{lm,k}$ diagrams of class III.

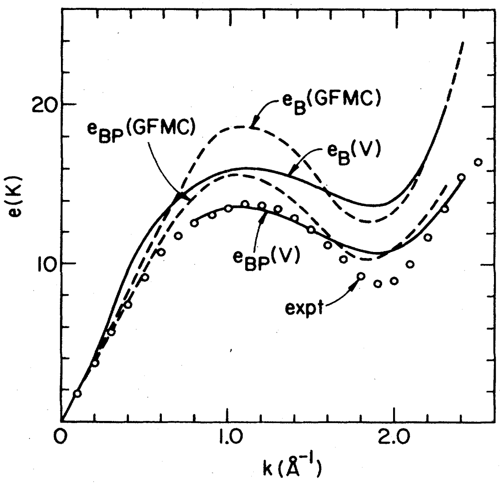

FIG. 17. Spectrum at zero pressure calculated with the variational (V) and GFMC $g(r)$.

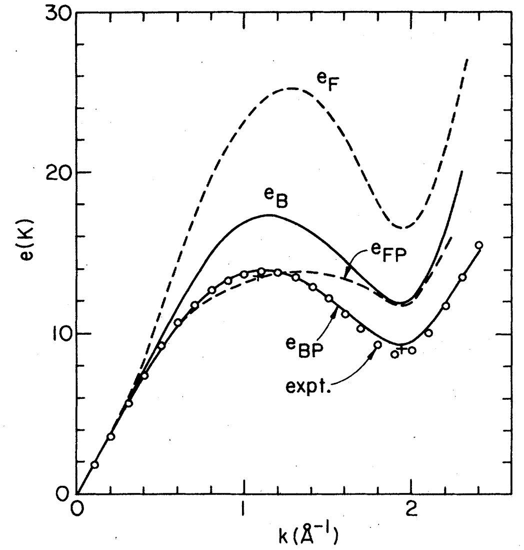

FIG. 18. Spectrum at zero pressure calculated with the experimental $S(k)$ and $g(r)$. RS maxon and roton energies are shown by plus signs.

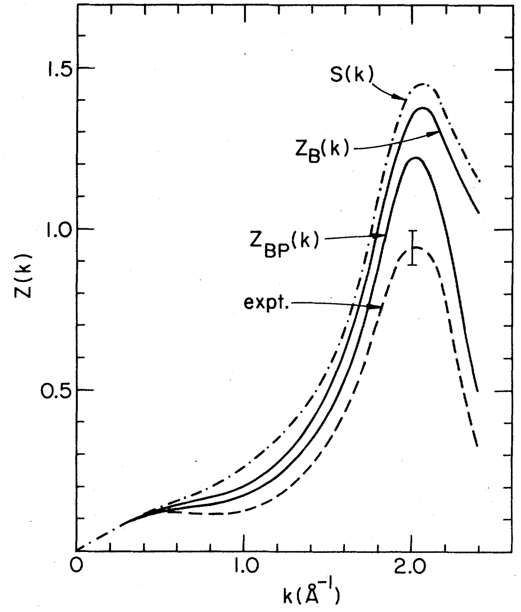

FIG. 19. Calculated $Z(k)$ for Feynman $[S(k)]$, FC $[Z_B(k)]$, and second-order CBF $[Z_{BP}(k)]$ phonons are compared with the experimental data (Ref. 14).

The $Z(k)$ obtained with this wave function is

$$Z(k)=\left[1+\tfrac{1}{2}\sum_{\vec{l}\,(\neq\vec{0},\vec{k})} A^2_{k,lm}\right]^{-1}\left\{\frac{\langle\Psi_0|\rho^\dagger(\vec{k})\rho_B(\vec{k})|\Psi_0\rangle}{\langle\Psi_0|\rho_B^\dagger(\vec{k})\rho_B(\vec{k})|\Psi_0\rangle^{1/2}}\right.$$
$$\left.+\tfrac{1}{2}\sum_{\vec{l}(\neq\vec{0},\vec{k})} A_{k,lm}[\langle\Psi_0|\rho^\dagger(\vec{k})\dot{\rho}_B(\vec{l})\dot{\rho}_B(\vec{m})|\Psi_0\rangle - N_{k,lm}\langle\Psi_0|\rho^\dagger(\vec{k})\rho_B(\vec{k})|\Psi_0\rangle/N_{kk}]/N^{1/2}_{lm,lm}\right\}^2 , \tag{4.7}$$

and the only new matrix element required to calculate it is the expectation value of $\dot{\rho}_B^\dagger(\vec{m})\dot{\rho}_B^\dagger(\vec{l})\rho(\vec{k})$. Its calculation is similar to that of $\dot{\rho}_B^\dagger(m)\dot{\rho}_B^\dagger(\vec{l})\rho_B(\vec{k})$ expectation value; one simply discards the terms with the wiggly line from $\rho_B(\vec{k})$.

The diagrams are classified as in the calculation of $N_{ml,k}$. We denote the contributions of diagrams of first, second, and third class by M_1, M_2, and M_3, respectively; there are no class four diagrams in this case. Thus, in the ETB approximation,

$$\langle\Psi_0|\dot{\rho}_B^\dagger(\vec{m})\dot{\rho}_B^\dagger(\vec{l})\rho(\vec{k})|\Psi_0\rangle=M_1+M_2+M_3 , \tag{4.8}$$

$$M_1=S(k)[S_B(l)S_B(m)-1] , \tag{4.9}$$

$$M_2=M_{2,j}+M_{2,n} ,$$

$$M_{2,j}=\tfrac{1}{2}S(k)\left[-\frac{\vec{l}\cdot\vec{m}}{m^2}\bar{I}_9(m)S_B(m)+\frac{\vec{k}\cdot\vec{l}}{k^2}\bar{I}_9(k)[S_B(m)-1]\right] , \tag{4.10}$$

$$M_3=S(k)\rho\int d^3r\, g(r)\eta^2(r)(\vec{m}\cdot\vec{r})(\vec{l}\cdot\vec{r})(e^{i\vec{m}\cdot\vec{r}}+e^{i\vec{l}\cdot\vec{r}}) . \tag{4.11}$$

TABLE II. Maxon and roton energies (in K) calculated with the experimental $S(k)$ compared with experiment at three densities corresponding to 0-, 10-, and 24-atm pressure.

	Maxon				Roton			
$\rho(\sigma^{-3})$	e_B	e_{BP}		e_{expt}	e_B	e_{BP}		e_{expt}
		BW	RS			BW	RS	
0.365	17.30	14.06	13.45	13.8	11.75	9.25	8.96	8.7
0.4017	19.59	15.65	14.68		11.60	8.76	8.45	7.9
0.4276	20.63	16.48	15.62	~15	11.07	8.08	7.75	7.1

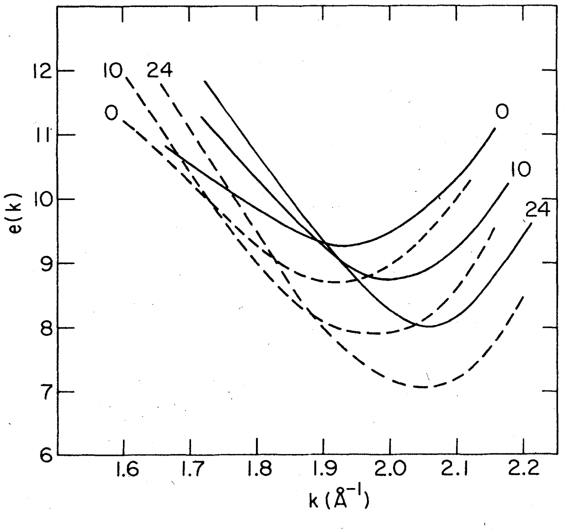

FIG. 20. Calculated $e_{\rm BP}(k)$ for rotons (solid lines) at 0-, 10-, and 24-atm pressure is compared with the experimental data (Ref. 15) shown by dashed lines.

V. RESULTS

The formalism developed by FC and in this work assumes that the $|\Psi_0\rangle$ is the correct ground state of the liquid. Hence we must use the exact distribution functions to calculate the spectrum. In this section we use two approximation for the pair distribution function $g(r)$; that obtained with variational calculations[10] and the one from presumably exact Green's function Monte Carlo (GFMC) calculations.[12] Both these microscopic approaches use a model Hamiltonian with the Aziz interatomic potential, which is believed to be quite realistic. They neglect three-body or higher-body forces. The variational calculations assume the form given by Eq. (2.20) for the wave function, but the functions f_{ij} and $f_{3,ijk}$ are not determined in a truly exact fashion. Due to finite-size effects, the "exact" GFMC calculations do not give the correct $S(k)$ in the $k \rightarrow 0$ limit. We correct the GFMC $S(k<0.4$ Å$^{-1})$ by hand. The $S(k)$ and $g(r)$ have been experimentally measured,[13] and the best choice is of course to use them. Most of the presented results are with this choice.

Secondly, tables of $g_{3,ijk}$ obtained in GFMC calculations are not available, and the g_3 is not known from experiments. Hence the Abe correction [Eqs. (2.2) and (2.22)] must be obtained from the variational calculations. More specifically we use the scaling constant in Eq. (2.17) and the $f_{3,ijk}$ from Ref. 10 to calculate the spectra with the experimental and the GFMC $g(r)$. The Abe correction has a small effect on the spectrum, and obtaining it from the variational calculations may not be a serious approximation.

The results reported here are obtained with the "full" calculations of $e_B(k)$ as described in Sec. II. However the second-order CBF corrections are calculated with the extended two-body approximation. The calculated spectra at equilibrium density are shown in Figs. 17 and 18, where $e_{\rm BP}$ and $e_{\rm FP}$ denote the results obtained with second-order Brillouin-Wigner (BW) perturbation theory using FC and Feynman phonon basis states, respectively. The $e_{\rm BP}$ is, as one might have expected, much closer to experiment. Differences between Rayleigh-Schrödinger (RS) and BW results give an indication of the convergence of the perturbation expansion. The RS and BW energies are given in Table II for the $e_{\rm BP}$. The difference between them is 0.3 and 0.6 K for the roton and maxon at the equilibrium density. These differences are about four times greater (1.0 and 3.0 K) for the $e_{\rm FP}$.

The spectrum obtained with the GFMC and the variational $g(r)$ have about 15% errors due to the inaccuracies in these calculations. The perturbative correction $e^{(2)}(k)$ obtained in calculations using variation, GFMC, and the experimental $g(r)$ is quite similar; the main differences appear in the $e_B(k)$. The main problems with the theoretical $S(k)$ appear to be in the region of the peak and

TABLE III. Calculated $e(k)$ and $Z(k)$.

	$P=0$ atm		$P=10$ atm		$P=24$ atm	
k (Å^{-1})	$e_{\rm BP}(k)$	$Z_{\rm BP}$	$e_{\rm BP}(k)$	$Z_{\rm BP}$	$e_{\rm BP}(k)$	$Z_{\rm BP}$
0.225	4.48	0.084	5.28	0.062	6.42	0.057
0.425	7.32	0.114	8.82	0.089	9.30	0.080
0.625	10.54	0.135	11.71	0.109	12.51	0.091
0.825	12.81	0.152	13.92	0.122	15.09	0.096
1.025	13.90	0.184	15.46	0.136	16.39	0.111
1.125	14.06	0.208	15.66	0.154	16.46	0.127
1.225	13.79	0.246	15.48	0.180	16.10	0.155
1.425	12.72	0.362	13.92	0.289	14.60	0.248
1.625	11.27	0.573	12.18	0.471	12.72	0.410
1.825	9.70	0.950	10.14	0.829	10.38	0.746
1.925	9.24	1.155	9.01	1.115	8.99	1.044
1.975	9.34	1.211	8.77	1.232	8.44	1.211
2.025	9.62	1.228	8.76	1.305	8.10	1.342
2.125	10.73	1.144	9.51	1.287	8.45	1.411
2.325	13.89	0.725	12.74	0.838	11.58	0.919

around $k \sim 1$ Å^{-1}.

The Z_k obtained in various approximations is compared with the data[14] in Fig. 19. It is given by $S(k)$ for the Feynman phonon. The results obtained for the FC phonon state shown by the curve labeled $Z_B(k)$, while the second-order BW calculation gives the curve labeled $Z_{\rm BP}(k)$. Unfortunately $Z_{\rm BP}(k)$ appears to be only half way between the $S(k)$ and the experiment. Thus the wave functions of our phonons are not very accurate.

The calculated spectra and Z at three densities, at which experimental data for $S(k)$ is available,[13] are given in Table III. The pressure dependence of the theoretical roton spectrum is compared with experiment[15] in Fig. 20. As the pressure is increased from 0 to 24 atm, the roton energy drops by 1.6 K. This decrease is underestimated by 25%, the theoretical roton energy drops by only 1.2 K.

ACKNOWLEDGMENTS

The authors would like to thank Professor C. E. Campbell for useful communication. This work was supported by the U.S. Department of Energy (Division of Material Sciences) under Grant No. DE-AC02-76ER01198.

---

[1] R. P. Feynman and M. Cohen, Phys. Rev. **102**, 1189 (1956).

[2] T. C. Padmore and C. V. Chester, Phys. Rev. A **9**, 1725 (1974).

[3] K. E. Schmidt and V. R. Pandharipande, Phys. Rev. B **21**, 3945 (1980).

[4] E. Feenberg, *Theory of Quantum Fluids* (Academic, New York, 1969).

[5] H. W. Jackson and E. Feenberg, Rev. Mod. Phys. **34**, 686 (1962).

[6] D. K. Lee and F. J. Lee, Phys. Rev. B **11**, 4318 (1975).

[7] C. C. Chang and C. E. Campbell, Phys. Rev. B **13**, 3779 (1976).

[8] Q. N. Usmani, B. Friedman, and V. R. Pandharipande, Phys. Rev. B **25**, 4502 (1982).

[9] K. E. Schmidt, M. A. Lee, M. H. Kalos, and G. V. Chester, Phys. Rev. Lett. **47**, 807 (1981); E. Manousakis, S. Fantoni, V. R. Pandharipande, and Q. N. Usmani, Phys. Rev. B **28**, 3770 (1983).

[10] Q. N. Usmani, S. Fantoni, and V. R. Pandaripande, Phys. Rev. B **26**, 6123 (1982).

[11] A. Miller, D. Pines, and P. Noziéres, Phys. Rev. **127**, 1452 (1962).

[12] M. H. Kalos, M. A. Lee, P. A. Whitlock, and G. V. Chester, Phys. Rev. B **24**, 115 (1981).

[13] H. N. Robkoff and R. B. Hallock, Phys. Rev. B **24**, 159 (1981), and Phys. Rev. B **25**, 1572 (1982).

[14] R. A. Cowley and A. D. B. Woods, Can J. Phys. **49**, 177 (1971).

[15] O. W. Dietrich, E. H. Graf, C. H. Huang, and L. Passell, Phys. Rev. A **5**, 1377 (1972).